The SensorOverlord predicts the accuracy of measurements with ratiometric biosensors

Julian A. Stanley, Sean B. Johnsen, and Javier Apfeld*

Biology Department, Northeastern University, Boston, MA, 02115, USA

* For correspondence: j.apfeld@northeastern.edu

Abstract

Two-state ratiometric biosensors change conformation and spectral properties in response to specific biochemical inputs. Much effort over the past two decades has been devoted to engineering biosensors specific for ions, nucleotides, amino acids, and biochemical potentials. The utility of these biosensors is diminished by empirical errors in fluorescence-ratio signal measurement, which reduce the range of input values biosensors can measure accurately. Here, we present a formal framework and a web-based tool, the SensorOverlord, that predicts the input range of two-state ratiometric biosensors given the experimental error in measuring their signal. We demonstrate the utility of this tool by predicting the range of values that can be measured accurately by biosensors that detect pH, NAD^+, NADH, NADPH, histidine, and glutathione redox potential. The SensorOverlord enables users to compare the predicted accuracy of biochemical measurements made with different biosensors, and subsequently select biosensors that are best suited for their experimental needs.

Introduction

Genetically encoded two-state ratiometric biosensors have revolutionized our ability to monitor a wide variety of biochemical species[1-8]. The development of these biosensors has enabled the visualization in real-time of the biochemical properties of live animals using fluorescence-ratio microscopy. However, the potential of these biosensors has not been fully realized because the empirical imprecision of their fluorescence-ratio signal measurements reduces the range of biochemical input values those biosensors can measure accurately.

The capacity to make accurate measurements with sensors is important because it enables observers to make confident predictions about the state of a system. Using a ther-

mometer that makes inaccurate temperature measurements can lead to incorrect predictions about the state of a physical system; for example, in predicting whether water will be a solid, a liquid, or a gas. Similarly, using a genetically encoded biosensor that makes inaccurate measurements can lead to incorrect predictions about the state of a biological system.

In our previous work in the nematode *C. elegans*, we deployed a mathematical framework that enabled us to map the fluorescence-ratio signal of the roGFP1-R12 biosensor into glutathione redox potential (E_{GSH}) values using prior information about our microscope's properties and the biosensor's spectral and biochemical properties[9,10]. Here, we extend that framework to determine how the precision of our fluorescence-ratio signal measurements with the roGFP1-R12 biosensor constrains the range of E_{GSH} values that can be measured accurately. We then generalize this extended framework for all two-state ratiometric biosensors with known spectral and biochemical properties. We demonstrate the utility of this new framework by: (i) determining the range of E_{GSH} values that we can measure accurately in live *C. elegans* with the roGFP1-R12 biosensor; (ii) quantifying how much that range of E_{GSH} values is expanded by increasing the precision of our imaging and image-analysis methods; (iii) identifying which biosensors are best suited for measuring accurately different ranges of E_{GSH}, pH, and the concentrations of nucleotides and amino acids; (iv) identifying underused biosensors; and (v) identifying where new biosensors are needed.

To help the community identify biosensors that are well-suited for their experimental needs, we developed a web-based tool, the SensorOverlord (https://www.sensoroverlord.org), that implements all of these analyses with a user-friendly interface.

Results

Predicting the accuracy of a glutathione redox potential biosensor. The human and *C. elegans* proteomes contain ~210,000 cysteine residues[11,12] and ~15% of these cysteines are reversibly oxidized[13]. These protein networks can be understood as markets where cysteines in proteins buy (*reduction*) and sell (*oxidation*) pairs of electrons only via a central broker, the abundant glutathione tripeptide[9], resulting in a single price for trading electrons that determines the oxidation of all cysteines in the network (Figure 1a). In chemical terms, this price is the glutathione redox potential (E_{GSH}): the Nernst potential that quantifies the balance between reduced and oxidized glutathione species. Measuring E_{GSH} is critical because cysteine oxidation modulates the function of hundreds of cytosolic proteins[14-20] which regulate a wide variety of cellular processes[20,21]. The mechanisms that regulate E_{GSH} *in vivo* remained largely unexplored until the development of the E_{GSH}-specific roGFP-family of genetically-encoded biosensors[10,22,23]. These GFP-derived biosensors include two cysteines that form a (reversible)

intramolecular disulfide bond upon oxidation, resulting in spectral changes that can be quantified via fluorescence-ratio microscopy (Figure 1b)[8]. We previously used the roGFP1-R12 biosensor to measure E_{GSH} in live *C. elegans*[9]. To map fluorescence-ratio (R) measurements into E_{GSH} values, we determined three conversion factors that quantify the properties of our imaging microscope and the spectral differences between the reduced and oxidized states of the biosensor (Supplementary Note 1). Measuring E_{GSH} instead of R enabled us to make predictions about how the oxidation state of the network of cysteines trading electrons with glutathione is influenced by genetic determinants and environmental factors[9]. However, those predictions require that E_{GSH} be measured accurately. Therefore, we set out to determine how the precision of our fluorescence-ratio microscopy influenced the range of E_{GSH} values we could measure accurately.

We first modeled how errors in fluorescence-ratio measurement influenced E_{GSH} errors. The conversion map from R to E_{GSH} is highly nonlinear (Figure 1c). As a result, the size of an E_{GSH} error depends not only on the size of the error in R but also on the value of R (Figure 1d): as R approaches its lower and upper bounds E_{GSH} errors increase rapidly (Supplementary Note 2). Thus, even a small difference between observed and true R values (R_{Obs} and R_{True}, respectively) can lead to a large difference between observed and true E_{GSH} values (E_{Obs} and E_{True}, respectively) (Figure 1d).

We then determined the size of our fluorescence-ratio measurement errors. We quantified the precision of our fluorescence-ratio measurements in live *C. elegans* expressing the roGFP1-R12 biosensor in the cytosol of the muscles of the pharynx, the feeding organ. This retrospective analysis of 10,572 images showed that our errors in R were proportional to R—that is, $R_{Obs} = R_{True} * (1 + error)$ (Supplementary Note 3). Within a given experiment, the size of the relative error in R was invariant over the range of all possible R values (Supplementary Note 3). The size of the relative error in R, however, varied up to three-fold between experiments (Supplementary Note 3). Differences in the proportion of animals moving during imaging accounted for most of the variation in the relative error in R across experiments (S.B.J., J.A.S., and J.A., manuscript in preparation). Our analysis indicated that, in a typical experiment, the median relative error in R was zero and 95% of the relative errors in R were in the interval (-2.8%, +2.8%) (Figure 1f). These 95% confidence bounds quantified the precision of our fluorescence-ratio measurements.

Last, we determined how the empirical precision of our fluorescence-ratio measurements influenced the accuracy of individual E_{GSH} observations. Knowing the precision of our R measurements enabled us to determine the 95% confidence bounds of E_{Obs} as a function of R_{True} (Figure 1d). Converting R_{True} into E_{True} produced a map of how the 95% confidence bounds of E_{Obs} varied as a function of E_{True} (Figure 1e). The maximum absolute difference between E_{True} and either the upper or lower 95% confidence bound of E_{Obs} represents the inaccuracy of our

E_{GSH} measurements (Figure 1g). Our mathematical modeling indicated that the precision of R measurements, the biochemical and biophysical properties of the biosensor, and the choice of excitation wavelengths used in our experiments all influenced the E_{GSH} values that we could measure most accurately (Supplementary Note 4). E_{GSH} inaccuracy rapidly increased as E_{True} moved farther away from that value.

This analysis enabled us to extract the range of E_{GSH} values that our biosensor was well-suited to measure at a given level of E_{GSH} inaccuracy (Figure 1g). For example, the range of E_{Obs} values we could measure with an inaccuracy of 2 mV was between -284 and -234 mV. This range encompassed all E_{GSH} values we observed in wild-type nematodes under normal conditions (-278 to -262 mV) and under oxidative stress (-278 to -250 mV)[9], indicating that our experimental set up was well-suited to measure the E_{GSH} values that *C. elegans* feeding muscles exhibited *in vivo*: 95% of the individual E_{GSH} observations deviated from their true value by less than 2 mV.

Balancing the need for accurate measurements with the constraints of microscopy. Our analytical framework provides a criterion for determining if it is possible to measure E_{GSH} accurately. Scientific needs demand accurate observations, but experimental approaches constrain the extent to which observations can be made accurately. The trade-off between these scientific and experimental constraints can be visualized in a phase diagram (Figure 2). The precision of R measurements determines the range of E_{GSH} values that is possible to measure at a specific inaccuracy level (Figure 2). For values outside that range, it is impossible to guarantee that an observation will be accurate. Scientific needs impose a maximum tolerable inaccuracy beyond which observations are too inaccurate and, therefore, not useful. Together, these constraints determine whether it is possible to measure E_{GSH} accurately (Figure 2).

Retrospectively increasing measurement accuracy with improved image analysis. To increase the range of E_{GSH} values that we could measure accurately, we set out to improve our image-analysis methods. Movement of live *C. elegans* during image acquisition lowers the precision of fluorescence-ratio measurements in individual pharyngeal muscles. In a typical experiment 21% of animals moved during imaging. We developed a new image-feature registration algorithm that corrects for displacement and deformation of the muscles along the anterior-posterior axis of the pharynx (S.B.J. and J.A., manuscript in preparation). This new image-analysis algorithm reduced the relative error in R along most positions in the pharynx, especially in the boundaries between adjacent muscles and in the muscles of the anterior and posterior bulbs. For example, in the pm7 muscles of the posterior bulb, the new algorithm reduced the interval with 95% of the relative errors in R from ±4.3% to ±2.6% in moving animals and from ±2.0% to ±1.9% in stationary animals. As a result, the new algorithm increased the

accuracy with which we could measure E_{GSH} and thereby expanded the range of E_{GSH} values that we could measure accurately in past experiments (Figure 3a).

Comparing glutathione redox potential biosensors. We determined the ranges of E_{GSH} values that we could have measured accurately had we used different biosensors. Theoretical modeling indicated that the accuracy of a biosensor is influenced by the choice of wavelengths used for biosensor excitation, and by the biosensor's dynamic range and midpoint-potential ($E^{0'}$, the price point where a biosensor is 50% likely to sell its electrons) (Supplementary Note 4). These biosensor physical and chemical properties vary among all existing roGFP-based biosensors (Supplementary Note 5). We estimated the conversion factors that map fluorescence-ratio measurements into E_{GSH} values for the eleven roGFP-based biosensors with known midpoint potentials and fluorescence spectra (Supplementary Note 5). This enabled us to determine the E_{GSH} inaccuracy we would expect to observe had we measured E_{GSH} in the feeding muscles of live *C. elegans* with each of those biosensors instead of roGFP-R12 (Figure 3b and Supplementary Note 5). This analysis enabled us to identify which biosensors would measure E_{GSH} most accurately under our experimental conditions: roGFP5 for E_{GSH} values below -297 mV, roGFP2 for E_{GSH} values from -296 mV to -258 mV, roGFP1-R12 for E_{GSH} values from -257 to mV to -240 mV, and roGFP1-iE for E_{GSH} values above -239 mV. We note that often many biosensors were predicted to have comparable accuracies (Figure 3b).

This analysis helped us identify underused biosensors. Neither roGFP3 nor roGFP5 has ever been used *in vivo*, yet we predict that these biosensors would be the most accurate biosensors for low E_{GSH} values such as those expected for the mitochondrial matrix. We currently disfavor roGFP5, even though this biosensor was predicted to be more accurate than roGFP3, because roGFP5 can potentially form more than one type of internal disulfide bridge due to its two additional cysteines; a better understanding of roGFP5's biochemistry is warranted given its potential utility.

Comparison of the predicted accuracy of biosensors originally designed for similar purposes enabled us to identify the variables that explain why one biosensor was predicted to be more accurate than another (Supplementary Note 6). For example, both roGFP1-iE and roGFP2-iL were designed to have higher midpoint potentials than previous roGFPs, making them more suitable for measuring the higher E_{GSH} values common in the endoplasmic reticulum[24,25]. However, while roGFP1-iE has a higher midpoint potential than roGFP2-iL, it is predicted to be more inaccurate than roGFP2-iL even for measuring higher E_{GSH} values. The higher dynamic range of roGFP2-iL makes it a more accurate E_{GSH} biosensor than roGFP1-iE.

Identifying where new glutathione redox potential biosensors are needed. We predicted the E_{GSH} inaccuracy that we would observe if we measured E_{GSH} in the feeding muscles of live

C. elegans with the most accurate biosensor for each E_{GSH} value. Using a phase diagram, we visualized the trade-off between our scientific need for accuracy and the experimental constraints imposed by the precision of our *R* measurements and the properties of existing biosensors (Figure 3c). This analysis indicated that we lack biosensors well-suited to measure E_{GSH} values above -177 mV or below -337 mV with at least 10 mV accuracy.

A general framework to predict the accuracy of two-state ratiometric biosensors. To establish a general criterion for determining whether a two-state biosensor is well-suited to measure its input accurately, we generalized the analysis framework for glutathione redox potential biosensors to all ratiometric two-state single-ligand-binding biosensors (Supplementary Notes 1, 5, 7). To demonstrate the utility of the generalized framework, we applied it to biosensors that measure pH and small molecules, including histidine, NAD^+, NADH, and NADPH. For each biosensor with known affinity constant and fluorescence spectra, we derived the conversion factors that map its fluorescence-ratio to pH or ligand concentration (Supplementary Notes 8, 9). We then determined the pH and ligand concentration ranges that each biosensor would be well-suited to measure accurately given the precision of our *R* measurements and selecting optimal excitation or emission filters for each biosensor (Figures 4a-b and Supplementary Notes 8, 9).

Comparison of the predicted accuracy of nine ratiometric pH biosensors identified optimal biosensors for pH measurement with dual-excitation red-fluorescent pH biosensors, dual-excitation green-fluorescent pH biosensors, and single-excitation dual-emission pH biosensors (Figure 4a). The NADH-specific Frex biosensor[6] had a higher predicted accuracy than the FrexH biosensor[6], as a result of its higher dynamic range (Figure 4b). The NADPH-specific iNAP1 biosensor[7] was predicted to more accurately measure NADPH concentration than the iNAP1-mCherry biosensor (Figure 4b). The iNAP1-mCherry biosensor sacrifices the iNAP1 dynamic range in one excitation band with pH-sensitive fluorescence, enabling pH-resistant NADPH measurement but lowering this biosensor's accuracy.

A web-based tool that predicts biosensor accuracy. To help the community find biosensors that are well-suited for their experimental needs, we developed the SensorOverlord toolkit. This open-source S4 class-based R package implements all the analyses described here. We also built a user-friendly web application, available at http://www.sensoroverlord.org (Figure 5). The SensorOverlord toolkit enables users to model how the precision of their fluorescence-ratio signal measurements and their microscopy configuration constrain the range of input values that their biosensor is well-suited to measure accurately.

Discussion

The SensorOverlord toolkit enables users to predict the accuracy of concentrations and chemical potentials derived from fluorescence ratio measurements with two-state biosensors. This tool enables users to select biosensors predicted to be most accurate for measuring specific ranges of biochemical values. The SensorOverlord also enables users to quantify the extent to which increasing the precision of their fluorescence-ratio measurements would increase the predicted accuracy of their biochemical measurements with an individual biosensor. Therefore, this tool can be used to quantify the accuracy gains resulting from improving experimental practices, and from refining image acquisition, registration, and analysis methods.

A wide variety of factors can influence the precision of fluorescence-ratio measurement. In our experience, the degree of immobilization of live specimens during image acquisition can influence the precision of fluorescence-ratio measurements by a factor of three, leading to large differences in the predicted accuracy of biochemical measurements. The SensorOverlord enables researchers to disclose the predicted accuracy of the concentrations and chemical potentials that they measure, simply by reporting the precision of their fluorescence-ratio measurements—similar to how manufacturers use tolerance ratings to disclose how often the quality of their products is expected to deviate from a standard. The broader scientific community may, in turn, adopt appropriate maximum tolerable inaccuracy standards for specific biochemical measurements.

We hope that the SensorOverlord motivates the development of new biosensors, microscopy techniques, and image-analysis methods, by enabling biosensor developers and users to quantify the accuracy gains that would result from modifying the biochemical and spectral properties of their biosensors and from increasing the precision of their fluorescence-ratio measurements.

Materials and Methods

Code availability. Mathematical modeling was performed in the R language and environment for statistical computing (v3.6.0)[26]. The web application and associated visualizations were developed with the R packages ggplot2 (v3.1.1)[27] and Shiny (v1.3.2)[28], respectively. Source code for the SensorOverlord is available at https://github.com/julianstanley/SensorOverlord.

Statistical analysis. All statistical analyses were performed in JMP (SAS). We tested for differences in the average *R* among groups using ANOVA. We used the Tukey HSD post-hoc test to determine which pairs of groups in the sample differ, in cases where more than two groups

were compared. We used least-squares regression to quantify the dependency on R of the absolute error in R and the absolute relative error in R.

Acknowledgements

We thank Jeff Bouffard, Jennifer Whangbo, Marianne Konikoff, Jodie Schiffer, Frank Servello, and Yuyan Xu for critical reading and detailed comments on our manuscript. We benefitted from discussions with members of Javier Apfeld's and Erin Cram's labs. Some strains were provided by the CGC, which is funded by NIH Office of Research Infrastructure Programs (P40 OD010440). The research was supported by a Northeastern TIER1 award and a National Science Foundation CAREER grant (1750065) to J.A.

Author Contributions

J.A.S. and J.A. conceived and designed the analysis framework. J.A.S. designed and implemented the SensorOverlord software. S.B.J. analyzed fluorescence-ratio measurement precision. J.A.S. and J.A. analyzed data, interpreted results and wrote the manuscript.

Competing Interests

The authors declare that no competing interests exist.

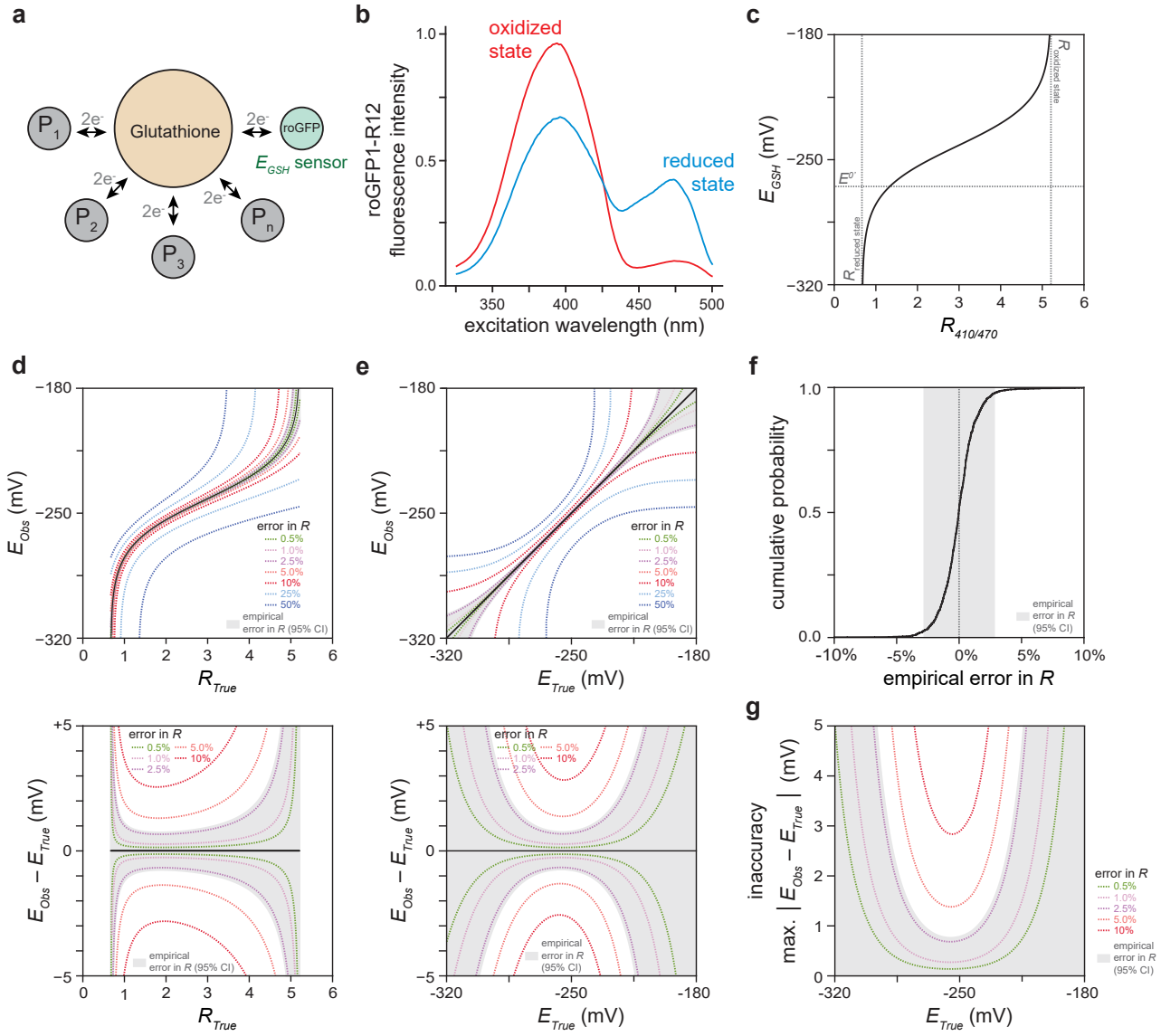

Figure 1. Determining the range of glutathione redox potential E_{GSH} values we can measure accurately with the roGFP1-R12 biosensor.

a. Glutathione redox potential (E_{GSH}) directs the oxidation of cysteines in hundreds of proteins in the same direction, resulting in their concerted regulation.

b. The reduced and oxidized states of the roGFP1-R12 biosensor have different fluorescence spectra[8], enabling E_{GSH} measurement via fluorescence-ratio (R) microscopy.

c. The conversion map from R to E_{GSH} is highly nonlinear. $R_{reduced\ state}$ and $R_{oxidized\ state}$ refer to the ratiometric emission of ensembles of reduced and oxidized biosensors, respectively. $E^{0'}$ is the

standard midpoint potential of the biosensor.

d. The top panel shows how measurement errors in R cause observed E_{GSH} values (E_{Obs}) to differ from the true E_{GSH} values (E_{True}) that would be observed if R was measured with no error (R_{True}). The bottom panel shows how the size of an E_{GSH} error ($E_{Obs} - E_{True}$) depends not only on the size of the error in R but also on the value of R. Each dotted curve corresponds to a different fold-change error in R. The shaded region corresponds the interval encompassing 95% of the predicted E_{Obs} values for each R_{True} value, given our empirical error in R.

e. Transforming the map from R_{True} to E_{True} in the top and bottom panels shown in **d** produces plots showing how errors in R influence the map from E_{True} to E_{Obs} (top panel) and how the size of an E_{GSH} error depends not only on the size of the error in R but also on the value of E_{True} (bottom panel). Each dotted curve corresponds to a different fold-change error in R. The shaded region shows the interval encompassing 95% of the predicted E_{Obs} values for each E_{True} value, given our empirical error in R.

f. Cumulative distribution of the empirical fold error in R in live *C. elegans* expressing the roGFP1-R12 biosensor in the cytosol of the anterior (pm3) muscles of the pharynx, the feeding organ. This error distribution was obtained by aggregating with equal weight the empirical fold error in R of five separate experiments (see Supplementary Note 3). 95% of the errors in R fall within the interval (-2.8%, +2.8%), shown shaded in gray. This interval quantifies the precision of our fluorescence-ratio measurements.

g. E_{GSH} measurement inaccuracy (the maximum absolute difference between E_{True} and E_{Obs}) decreases with increased precision of R measurement. Each dotted curve corresponds to a different precision of R measurement. The shaded region shows the interval encompassing 95% of the predicted E_{GSH} measurement inaccuracies for each E_{True} value, given our empirical error in R.

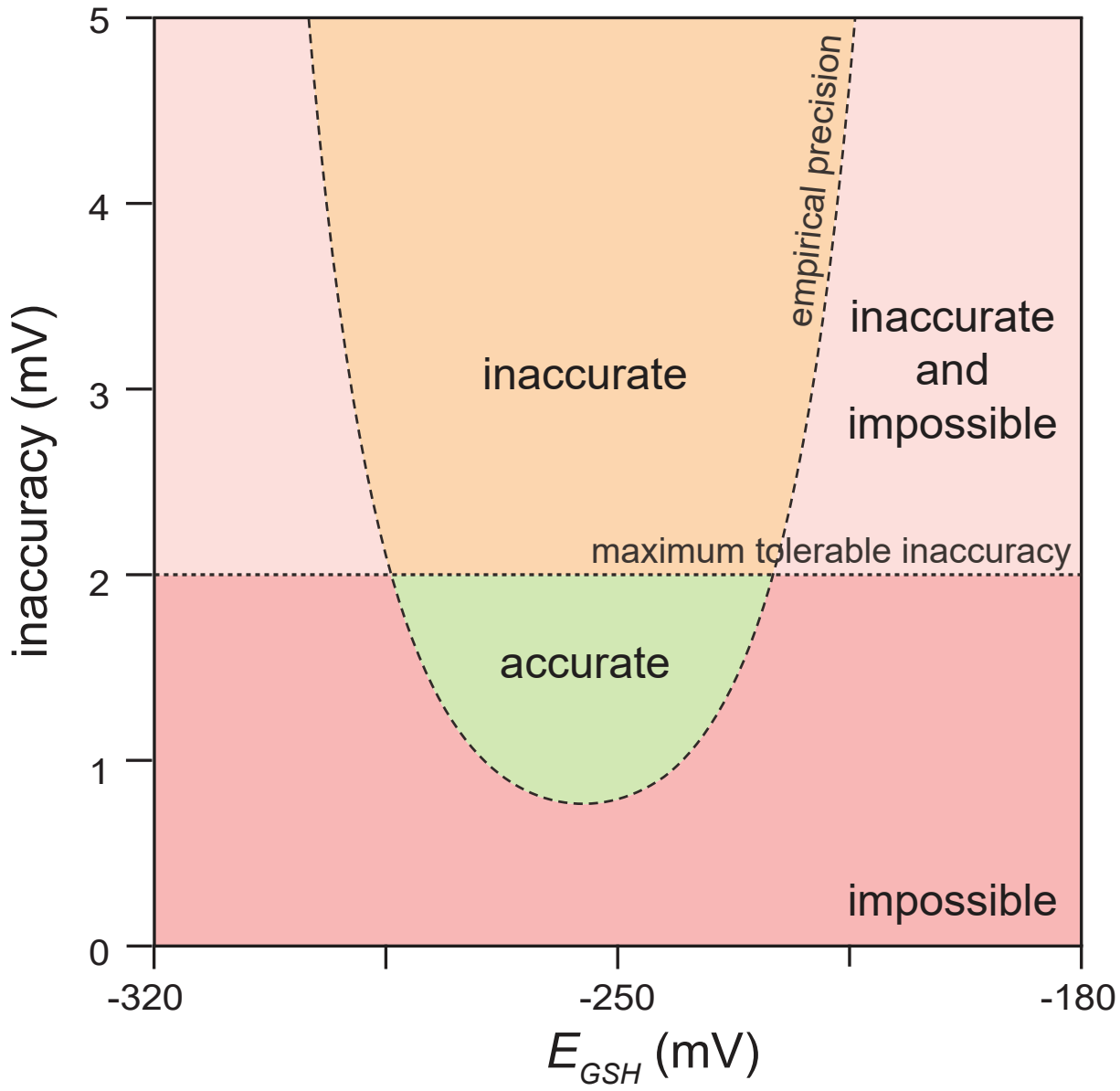

Figure 2. Balancing the need for accurate measurements with the constraints of microscopy.

The empirical precision of our *R* measurements determines the range of E_{GSH} values that is possible to measure at a specific inaccuracy level. Values outside that range are impossible to measure accurately (red and light red regions). Scientific needs impose a maximum tolerable inaccuracy beyond which observations are too inaccurate and, therefore, not useful (light red and orange regions). Together, these constraints determine whether it is possible to accurately measure E_{GSH} (green region).

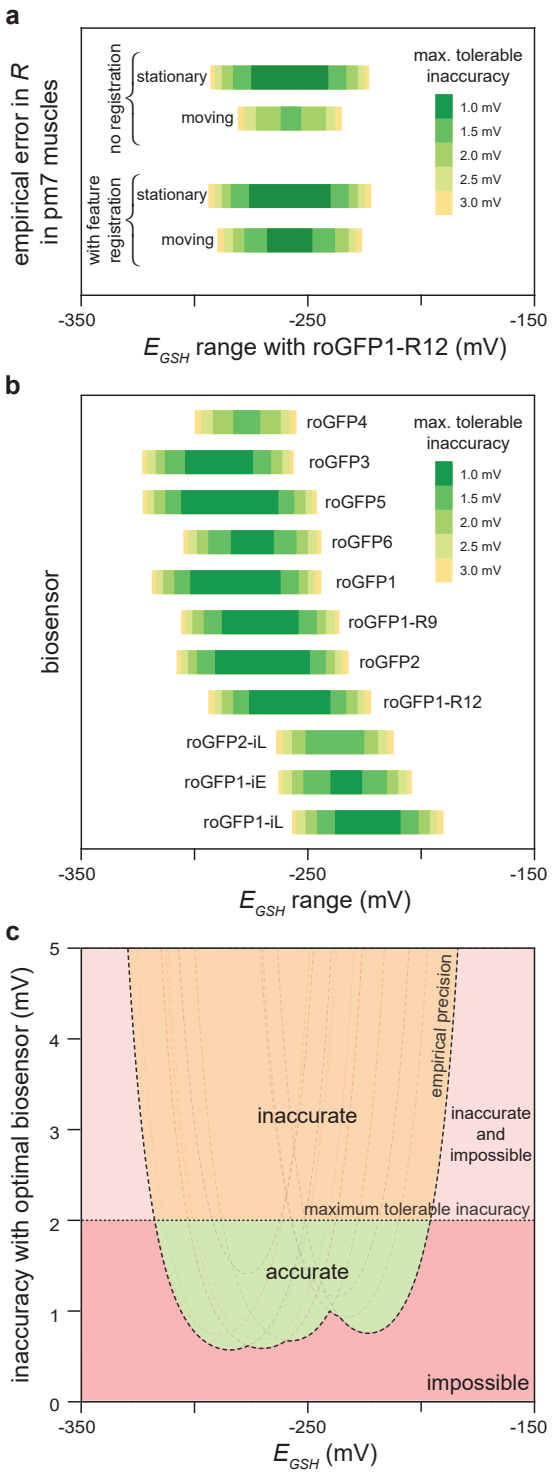

Figure 3. Predicted accuracy of glutathione redox potential biosensors.

a. Predicted accuracy gains from improved image analysis in the pm7 (posterior) feeding muscles of live *C. elegans* expressing the roGFP1-R12 biosensor. Animals that moved during image acquisition showed a higher *R* measurement error than stationary animals. A feature-registration algorithm increased the precision of *R* measurements, retrospectively expanding the

range of E_{GSH} values that we could measure accurately. The colored bars denote the range of E_{GSH} values where we have 95% confidence that an individual E_{GSH} observation would deviate from its true value by less than the error denoted by the color of the bar.

b. Predictions of the ranges of E_{GSH} values that we expect to measure accurately in pm3 pharyngeal muscles with eleven roGFP-based biosensors given the empirical precision of our R measurements. Coloring of bars as in panel **a**.

c. The empirical precision of our R measurements determines the range of E_{GSH} values that would be possible to measure at a specific inaccuracy level if we measured E_{GSH} in the pharyngeal muscles of live *C. elegans* with the most accurate roGFP biosensor for each E_{GSH} value. Values outside that range are impossible to measure accurately (red and light red regions). Scientific needs impose a maximum tolerable inaccuracy beyond which observations are too inaccurate and, therefore, not useful (light red and orange regions). Together, these constraints determine whether it is possible to accurately measure E_{GSH} with the eleven roGFP biosensors (green region). The dotted curves correspond to the predicted E_{GSH} inaccuracies of each of the eleven roGFP biosensors shown in **b**, given the precision of our R measurements.

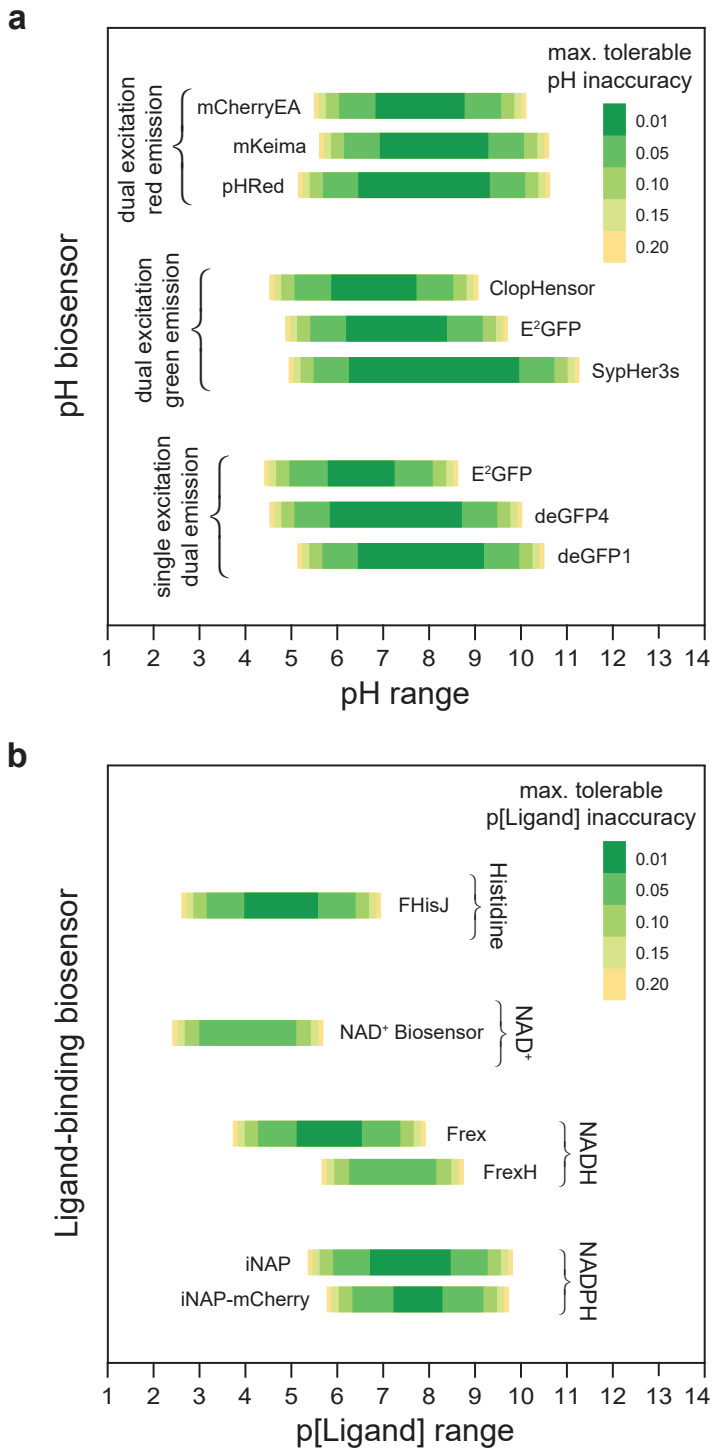

Figure 4. Predicted accuracy of pH and ligand-binding biosensors.

Predictions of the ranges of pH (panel **a**), and histidine, NAD^+, NADH, and NADPH values (panel **b**) that we expect to measure accurately in pm3 pharyngeal muscles with existing biosensors given the empirical precision of our *R* measurements and selecting optimal excitation or emission filters for each biosensor. The E^2GFP biosensor can be used in two different mo-

dalities, dual-excitation green-fluorescence and single-excitation dual-emission. Differences in the predicted pH inaccuracy of this biosensor under each imaging modality arise from the differences between the values in each imaging modality of this biosensor's overall dynamic range and dynamic range in the second wavelength (Supplementary Note 8). The colored bars denote the range of values of the biosensor's biochemical input where we have 95% confidence that an individual observation would deviate from its true value by less than the error denoted by the color of the bar. p[Ligand] is the negative base 10 logarithm of the Molar concentration of the biosensor's ligand.

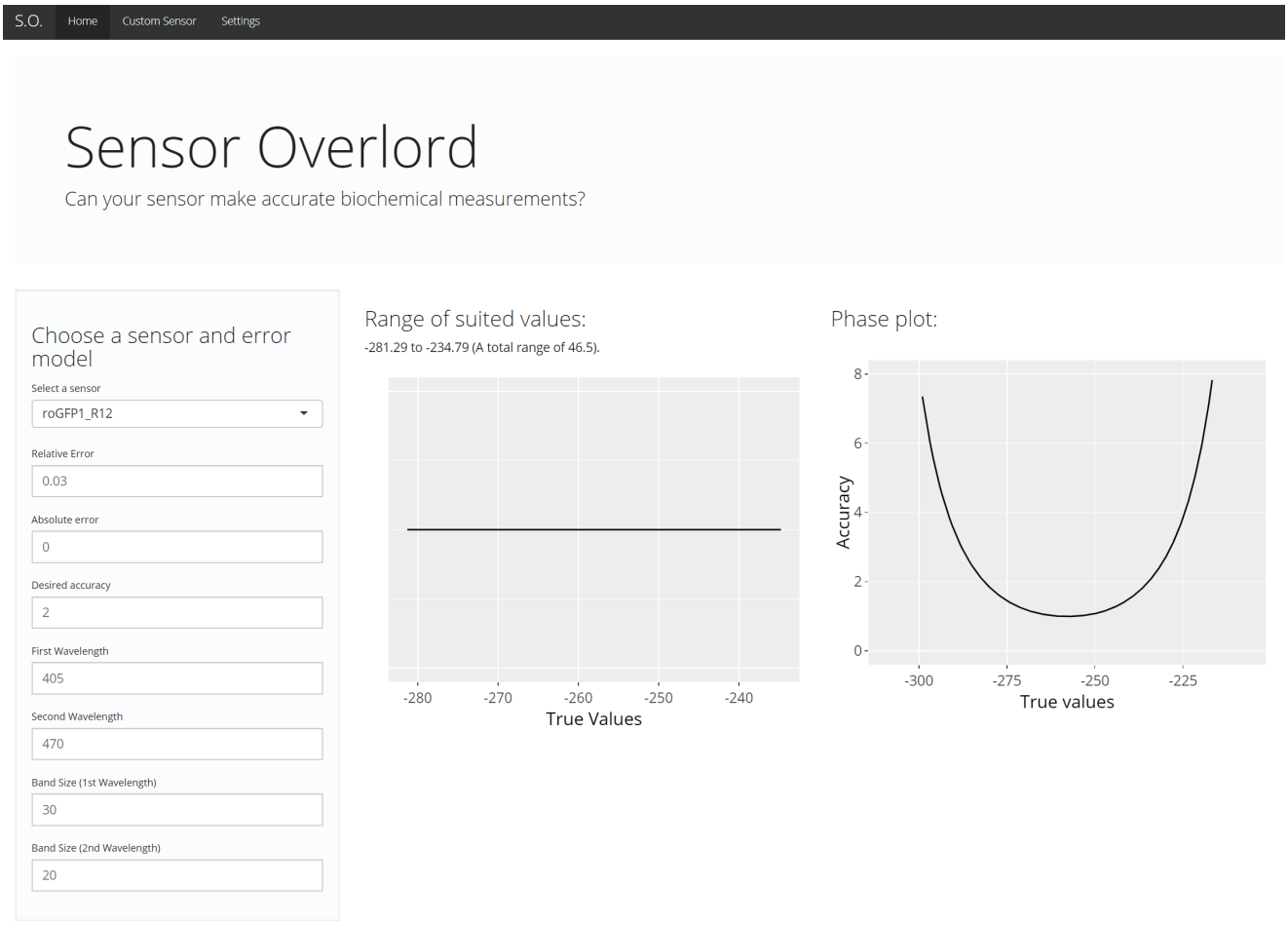

Figure 5. SensorOverlord web application.

The SensorOverlord toolkit enables users to model how the range of input values that their biosensor is well-suited to measure accurately is constrained by the user's fluorescence-ratio signal measurement precision and microscopy configuration.

References

1 Hanson, G. T. *et al.* Investigating mitochondrial redox potential with redox-sensitive green fluorescent protein indicators. *J Biol Chem* **279**, 13044-13053 (2004).

2 Tantama, M., Hung, Y. P. & Yellen, G. Imaging intracellular pH in live cells with a genetically encoded red fluorescent protein sensor. *J Am Chem Soc* **133**, 10034-10037 (2011).

3 Poburko, D., Santo-Domingo, J. & Demaurex, N. Dynamic regulation of the mitochondrial proton gradient during cytosolic calcium elevations. *J Biol Chem* **286**, 11672-11684 (2011).

4 Hu, H. *et al.* A genetically encoded toolkit for tracking live-cell histidine dynamics in space and time. *Scientific reports* **7**, 43479 (2017).

5 Cambronne, X. A. *et al.* Biosensor reveals multiple sources for mitochondrial NAD(+). *Science* **352**, 1474-1477 (2016).

6 Zhao, Y. *et al.* Genetically encoded fluorescent sensors for intracellular NADH detection. *Cell Metab* **14**, 555-566 (2011).

7 Tao, R. *et al.* Genetically encoded fluorescent sensors reveal dynamic regulation of NADPH metabolism. *Nat Methods* **14**, 720-728 (2017).

8 Cannon, M. B. & Remington, S. J. Re-engineering redox-sensitive green fluorescent protein for improved response rate. *Protein Sci* **15**, 45-57 (2006).

9 Romero-Aristizabal, C., Marks, D. S., Fontana, W. & Apfeld, J. Regulated spatial organization and sensitivity of cytosolic protein oxidation in *Caenorhabditis elegans*. *Nature communications* **5**, 5020 (2014).

10 Meyer, A. J. & Dick, T. P. Fluorescent protein-based redox probes. *Antioxid Redox Signal* **13**, 621-650 (2010).

11 Jones, D. P. Radical-free biology of oxidative stress. *Am J Physiol Cell Physiol* **295**, C849-868 (2008).

12 Moosmann, B. & Behl, C. Mitochondrially encoded cysteine predicts animal lifespan. *Aging Cell* **7**, 32-46 (2008).

13 Hansen, R. E., Roth, D. & Winther, J. R. Quantifying the global cellular thiol-disulfide status. *Proc Natl Acad Sci U S A* **106**, 422-427 (2009).

14 Gilbert, H. F. Biological disulfides: the third messenger? Modulation of phosphofructokinase activity by thiol/disulfide exchange. *J Biol Chem* **257**, 12086-12091 (1982).

15 Gilbert, H. F. Molecular and cellular aspects of thiol-disulfide exchange. *Adv Enzymol Relat Areas Mol Biol* **63**, 69-172 (1990).

16 Corcoran, A. & Cotter, T. G. Redox regulation of protein kinases. *FEBS J* **280**, 1944-1965 (2013).

17 Fuller, W. *et al.* Regulation of the cardiac sodium pump. *Cell Mol Life Sci* **70**, 1357-1380 (2013).

18 Yang, Y., Jin, X. & Jiang, C. S-glutathionylation of ion channels: insights into the regulation of channel functions, thiol modification crosstalk and mechanosensing. *Antioxid Redox Signal* **6**, 937-951 (2013).

19 de Keizer, P. L., Burgering, B. M. & Dansen, T. B. Forkhead box o as a sensor, mediator, and regulator of redox signaling. *Antioxid Redox Signal* **14**, 1093-1106 (2011).

20 Pastore, A. & Piemonte, F. S-Glutathionylation signaling in cell biology: progress and prospects. *Eur J Pharm Sci* **46**, 279-292 (2012).

21 Sakai, J. *et al.* Reactive oxygen species-induced actin glutathionylation controls actin dynamics in neutrophils. *Immunity* **37**, 1037-1049 (2012).

22 Meyer, A. J. *et al.* Redox-sensitive GFP in Arabidopsis thaliana is a quantitative biosensor for the redox potential of the cellular glutathione redox buffer. *The Plant journal : for cell and molecular biology* **52**, 973-986 (2007).

23 Schwarzlander, M. *et al.* Confocal imaging of glutathione redox potential in living plant cells. *J Microsc* **231**, 299-316 (2008).

24 Lohman, J. R. & Remington, S. J. Development of a family of redox-sensitive green fluorescent protein indicators for use in relatively oxidizing subcellular environments. *Biochemistry* **47**, 8678-8688 (2008).

25 Aller, I., Rouhier, N. & Meyer, A. J. Development of roGFP2-derived redox probes for measurement of the glutathione redox potential in the cytosol of severely glutathione-deficient rml1 seedlings. *Front Plant Sci* **4**, 506 (2013).

26 R_Core_Team. (R Foundation for Statistical Computing, Vienna, Austria., 2018).

27 Wickham, H. *Ggplot2 : elegant graphics for data analysis*. (Springer, 2009).

28 Shiny: Web Application Framework for R v. R package version 1.0.3 (2017).